



# OPEN Machine learning-based interpretation of non-contrast feature tracking strain analysis and T1/T2 mapping for assessing myocardial viability

Amir Ghaffari Jolfayi<sup>1</sup>, Alireza Salmanipour<sup>1</sup>, Kiyam Heshmat-Ghahdarijani<sup>1,2</sup>, Mohammad Hossein Mozafary Bazargany<sup>1</sup>, Amir Azimi<sup>1</sup>, Pirouz Pirouzi<sup>1</sup> & Ali Mohammadzadeh<sup>1</sup>✉

Assessing myocardial viability is crucial for managing ischemic heart disease. While late gadolinium enhancement (LGE) cardiovascular magnetic resonance (CMR) is the gold standard for viability evaluation, it has limitations, including contraindications in patients with renal dysfunction and lengthy scan times. This study investigates the potential of non-contrast CMR techniques—feature tracking strain analysis and T1/T2 mapping—combined with machine learning (ML) models, as an alternative to LGE-CMR for myocardial viability assessment. A retrospective analysis was conducted on 79 patients with myocardial infarction (MI) 2–4 weeks post-event. Patients with prior ischemia or poor imaging quality were excluded to ensure robust data acquisition. Various ML algorithms were applied to data from LGE-CMR and non-contrast CMR techniques. Random forest (RF) demonstrated the highest predictive accuracy, with area under the curve (AUC) values of 0.89, 0.90, and 0.92 for left anterior descending (LAD), right coronary artery (RCA), and left circumflex (LCX) coronary artery territories, respectively. For the LAD territory, RF, k-nearest neighbors (KNN), and logistic regression were the top performers, while RCA showed the best results from RF, neural networks (NN), and KNN. In the LCX territory, RF, NN, and logistic regression were most effective. The integration of T1/T2 mapping and strain analysis significantly enhanced myocardial viability prediction, positioning these non-contrast techniques as promising alternatives to LGE-CMR. ML models, particularly RF, provided superior diagnostic accuracy across coronary territories. Future studies should validate these findings across diverse populations and clinical settings.

**Keywords** Cardiovascular magnetic resonance, Feature tracking strain analysis, T1/T2 mapping, Myocardial viability

Ischemic heart disease (IHD) remains a leading cause of global morbidity and mortality, necessitating accurate diagnostic and prognostic tools for optimal patient management<sup>1,2</sup>. Cardiovascular magnetic resonance (CMR) imaging, particularly through late gadolinium enhancement (LGE), has established itself as the gold standard for assessing myocardial viability and fibrosis. LGE enables precise discrimination between ischemic and non-ischemic etiologies, providing crucial information for clinical decision-making regarding revascularization strategies and risk stratification<sup>3–5</sup>. However, this technique presents notable limitations, including contraindications in patients with kidney disease or contrast allergies, extended scan times due to the required 10–15-minute delay for contrast retention, and inability to provide comprehensive functional insights<sup>2,5</sup>.

The growing need for alternative diagnostic approaches has sparked interest in contrast-free techniques that could potentially reduce scan times, decrease costs, and improve CMR accessibility. Novel methods such as feature tracking (FT) strain analysis and T1/T2 mapping have emerged as promising gadolinium-free approaches for cardiac phenotyping<sup>2,6,7</sup>. While preliminary studies have demonstrated encouraging results, with research by

<sup>1</sup>Cardiovascular Research Center, Rajaie Cardiovascular, Medical, and Research Center, University of Medical Sciences, Tehran, Iran. <sup>2</sup>Heart Failure Research Center, Cardiovascular Research Institute, Isfahan University of Medical Sciences, Isfahan, Iran. ✉email: mralimohammadzadeh@yahoo.com

Tantawy et al. showing the capability of FT-CMR to differentiate between viable and non-viable segments<sup>6</sup> and Dastidar et al. highlighting the potential of native T1 mapping for viability assessment<sup>7</sup>, most investigations have been limited by isolated parameter analysis or small sample sizes.

The rapid advancement of artificial intelligence (AI) in cardiovascular imaging has opened new avenues for improving diagnostic accuracy and efficiency<sup>5</sup>. AI-based approaches have demonstrated significant utility across various CMR applications, including automated image acquisition, reconstruction, and analysis, while providing valuable diagnostic and prognostic information<sup>8</sup>. Recent developments in non-contrast CMR examinations supported by AI models have shown promising results in detecting myocardial infarction<sup>2,9–11</sup>. However, the application and validation of these approaches in comprehensive myocardial viability assessment across different segments and coronary artery territories remain largely unexplored.

This study aims to evaluate the combined efficacy of FT strain analysis and T1/T2 mapping integrated with machine learning (ML) pattern recognition techniques for predicting myocardial viability. By conducting a systematic comparison between these non-contrast methods and the established LGE technique, we seek to determine their relative diagnostic accuracy and potential advantages in clinical practice. This investigation represents a crucial step toward developing more accessible, efficient, and comprehensive approaches to myocardial viability assessment, potentially transforming the current paradigm of cardiac imaging diagnostics.

## Method and materials

### Study design

This study was conducted as a retrospective analysis of patients with myocardial infarction (MI) who underwent viability studies using LGE CMR two to four weeks post-MI. The primary aim was to assess the efficacy of FT strain analysis and T1/T2 mapping, in conjunction with ML, for predicting myocardial viability compared to LGE. A summary of the study method is demonstrated in Fig. 1.

### Study population

This retrospective study included patients with ST-segment elevation MI who underwent LGE CMR for viability assessment within the subsequent two to four weeks, from January 2020 to December 2021. The research was conducted in accordance with the Declaration of Helsinki and received approval from the Ethics Committee at the Rajaie Cardiovascular Medical and Research Center. The requirement of informed consent was waived by the Institutional Ethics Committee because it was a retrospective study. All methods were performed in accordance with the relevant guidelines and regulations. The study population was selected from a database of MI patients, ensuring a comprehensive collection of clinical and imaging data for robust analysis.

### Inclusion and exclusion criteria

The inclusion criteria comprised patients aged 18 years or older with a diagnosis of ST-segment elevation MI confirmed by clinical, biochemical, and electrocardiographic criteria who completed an LGE CMR viability study two to four weeks post-MI.

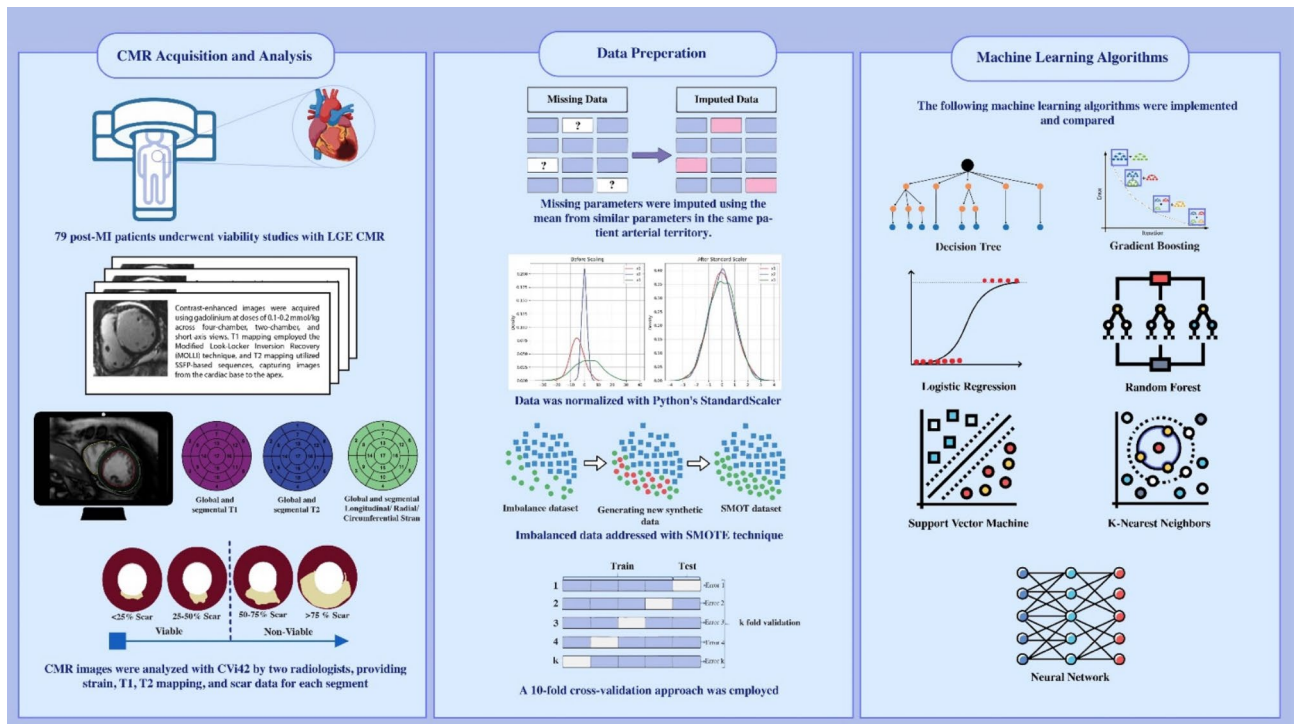


Fig. 1. Graphical Abstract. Overview of the study methodology.

Exclusion criteria included patients with contraindications to CMR, such as implanted metallic devices, incomplete or poor-quality imaging data, previous history of coronary artery bypass grafting (CABG) or other significant cardiac surgeries before the index MI and severe comorbidities that could impact survival or imaging outcomes. Patients were also excluded if they had undergone other forms of viability assessment, such as positron emission tomography (PET), to avoid confounding results.

### CMR imaging acquisition

CMR acquisition using the Sola MRI, a 1.5 Tesla XA20 with a 32-channel setup, involves a detailed protocol to ensure high-quality imaging, particularly for LGE. Initially, contrast is administered with a gadolinium-based agent at a dose ranging from 0.1 to 0.2 mmol/kg. Imaging begins in multiple planes, including four-chamber, two-chamber, and short-axis (SA) views. The field of view (FOV) is set to 300 mm, with a slice thickness of 6 mm across six slices. Following contrast administration, initial images are captured within 1 to 3 min to assess early contrast distribution with an inversion time (TI) greater than 400 ms. Subsequently, LGE images are acquired more than 10 min post-contrast to highlight areas of myocardial fibrosis or scarring, ensuring optimal tissue characterization and diagnostic accuracy.

#### *Data preprocessing by CVi42*

After acquiring the CMR on the Sola MRI (1.5 Tesla XA20, 32-channel), the digital imaging and communications in medicine (DICOM) images are exported for further analysis. The images are imported into CVi42 (Circle Cardiovascular Imaging Inc, Calgary, Canada) for the assessment of global longitudinal strain (GLS), global circumferential strain (GCS), and global radial strain (GRS). These parameters can detect subtle abnormalities in cardiac mechanics. Additionally, CVi42 supports T1 and T2 mapping, which are vital for tissue characterization. T1 mapping enables the assessment of myocardial fibrosis and extracellular volume, while T2 mapping is used to detect edema and inflammation. These advanced analyses help diagnose various cardiac conditions and monitor disease progression or response to therapy. Images were excluded from the study if they were suboptimal or non-diagnostic due to artifacts or signal loss that impaired accurate interpretation by the observers.

#### *T1 mapping*

T1 mapping is a crucial parameter for myocardial tissue characterization in CMR imaging. It is a promising tool for detecting myocardial abnormalities without gadolinium-based contrast agents. The myocardial T1 relaxation time reflects changes in the intracellular and extracellular components of the myocardium. Various pathologies affect the T1 values, such as collagen deposition (myocardial fibrosis), water (edema and inflammation), lipids (Fabry disease), and iron (hemosiderosis). T1 maps are generated from a series of T1-weighted images, with each pixel representing a specific T1 value, allowing precise quantification of tissue characteristics. T1 mapping can be conducted using several acquisition methods, with the modified look-locker inversion recovery (MOLLI) sequence commonly used, as in our study. At least three SA images are acquired from the base to the apex of the heart. Dedicated CMR software is used for quantifying T1 map images, where contours can be drawn manually or using automated features. Native T1 values are obtained by manually drawing a region of interest (ROI) on specific myocardial areas or by presenting the data in an AHA segmentation format. Normal myocardial native T1 reference ranges acquired using the MOLLI method have been reported to be  $930 \pm 21$  ms at 1.5 Tesla (Fig. 2).

#### *T2 mapping*

Similar to T1 values, T2 values represent a global signal from both intracellular and extracellular compartments. Each tissue type has a normal range of T2 values, and increased T2 values typically indicate elevated water content. Thus, myocardial edema (inflammation) is the main pathology resulting in increased T2 values. T2 mapping sequences are instrumental in detecting myocardial edema in patients with acute MI and myocarditis. Normal myocardial T2 values acquired using steady-state free precession (SSFP)-based sequences have been reported to be  $52.18 \pm 3.4$  ms at 1.5 Tesla (Fig. 2).

#### *Feature tracking for strain analysis*

Myocardial strain measures the deformation of the myocardium between relaxed and contracted states<sup>12</sup>. In ischemic heart disease, strain outperforms known risk markers like left ventricular (LV) ejection fraction or infarct size in predicting major adverse cardiac events<sup>13</sup>.

Several CMR strain techniques are available, including Tagging, displacement encoding with stimulated echoes (DENSE), and strain encoding (SENC), which require dedicated sequences. However, the most commonly used technique is FT, which processes routinely acquired cine SSFP MR images<sup>13,14</sup>. FT post-processing involves defining the endocardial and epicardial borders on short- and long-axis cine images and delineating the ventricular long axis at end-systole and end-diastole<sup>13,15</sup>. This allows the measurement of circumferential, longitudinal, and radial strain parameters (GLS, GCS, GRS). These steps can be done rapidly using artificial intelligence (AI) features of post-processing software.

Strain values can be displayed for the entire heart (global), at the section level (basal, mid, apical), by AHA segments, or within a specific ROI. Polar maps can display strain metrics in all 17 segments, and color-coded strain data can be overlaid on cine SSFP images for enhanced visualization (Fig. 3).

### Statistical analysis

#### *Excluding or imputing missing values*

Prior to conducting the machine learning analysis, we evaluated T1 and T2 mapping alongside strain feature tracking to maintain optimal data quality. Patients were excluded from the analysis if more than one segment within a given territory contained missing values. For cases with a single missing value in T1, T2, longitudinal,

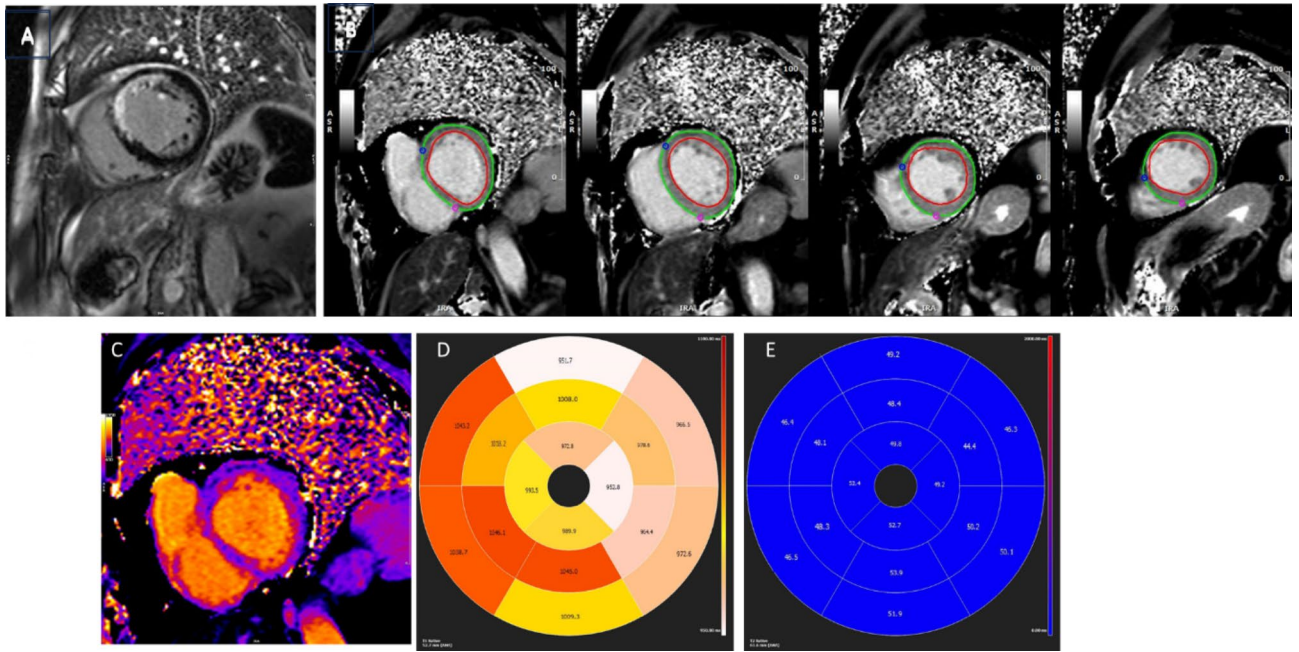


**Fig. 2.** Viability assessment in a 57-year-old man with LAD territory MI in STEMI. (A) Transmural LGE in base to midpart of the anteroseptal wall of LV. (B) Contouring of the LV wall for T1 and T2 evaluation. (C) High T1 values (T1 = 1043 ms) in the base to mid-segment of the anteroseptal LV wall due to septal fibrosis. (D) Polar map of T1-weighted LV wall showing an increased T1 value in the septal wall. (E) Polar map of T2-weighted LV wall showing normal T2 values in the septal wall (T2 = 48 ms).

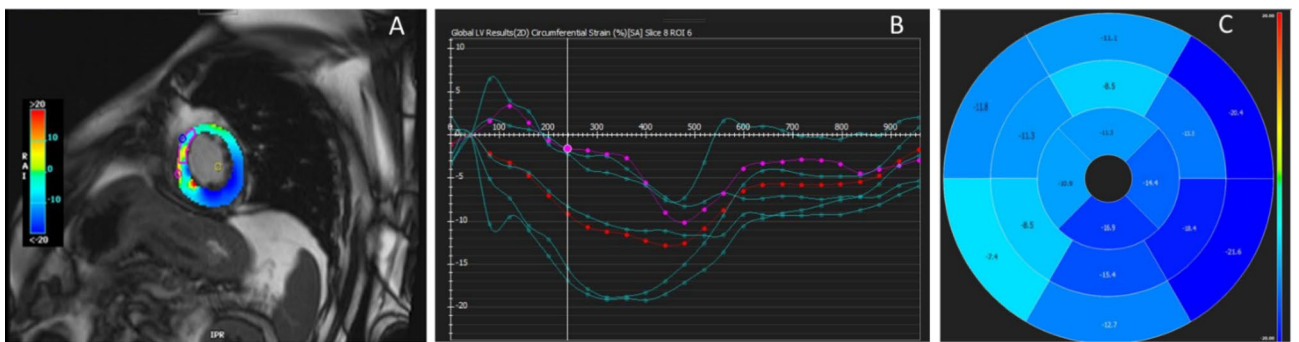


**Fig. 3.** A 57-year-old man with LAD territory MI. (A) Imaging depicting color-coded strain at mid-SAX. (B) Graph showing reduced circumferential strain in a specific ROI (mid-anteroseptal LV wall). (C) Polar map of circumferential strain values.

radial, or circumferential strain, the missing value was imputed by averaging the values of adjacent segments within the same territory. This approach replaced missing data with the mean of available values from the corresponding group, as demonstrated below.

$$\hat{x}_{ij} = \frac{1}{n_i} \sum x_{ij} \neq NA$$

$\hat{x}_{ij}$ : imputed value for the missing value,  $n_i$ : the number of non-missing values in group  $i$ ,  $x_{ij}$ : the observed value in group  $i$  variable  $j$ , NA denotes missing values.

*Normalization*

Normalization using StandardScaler in Python involves transforming the features of a dataset so that they have a mean of 0 and a standard deviation of 1. This standardization ensures that each feature contributes equally to the analysis, which can improve the performance of many ML algorithms. The normalization formula applied is:

$$z = \frac{x - \mu}{\sigma}$$

$x$  represents the original feature value,  $\mu$  is the mean of the feature, and  $\sigma$  is the standard deviation of the feature. This process adjusts the data to a common scale without distorting differences in the ranges of values, ensuring consistent and reliable analysis.

#### *Synthetic minority over-sampling technique (SMOTE)*

The synthetic minority over-sampling technique (SMOTE) is a technique for addressing class imbalance in datasets, particularly where one class predominates, potentially skewing classifier performance. SMOTE works by selecting a minority class instance, identifying its  $k$ -nearest minority class neighbors, and creating synthetic instances along the line segments connecting the instance and its neighbors. The formula for generating a synthetic instance is:

$$X_{new} = X_i + \lambda (X_j - X_i)$$

Here,  $X_i$  represents a minority class instance,  $X_j$  denotes one of its  $k$ -nearest neighbors ( $k=5$ ), and  $\lambda$  is a random number between 0 and 1.

In our study, SMOTE was applied to ensure the training dataset was balanced, thereby improving the classifier's ability to handle imbalanced data effectively.

#### *Data set splitting and ten-fold cross-validation*

A 10-fold cross-validation approach was employed to ensure robust evaluation and prevent overfitting. This method involved dividing the dataset into ten subsets, using nine for training and one for testing in each iteration, ensuring that each subset was used for testing only once.

$$CV_{error} = \frac{1}{k} \sum_{i=1}^k error_i$$

#### *Machine learning algorithms*

The following ML algorithms were implemented and compared: decision tree, gradient boosting, logistic regression, naive bayes, random forest (RF), support vector machine (SVM), K-Nearest Neighbors (KNN), and Neural Network (fully connected). Each algorithm was tuned using grid search to optimize hyperparameters and enhance performance.

#### *Resources and requirements*

For our machine learning tasks, we utilized an M2 MacBook Pro device powered by the Apple M2 chip, featuring an 8-core CPU and a 10-core GPU, with 16GB of unified memory, which efficiently handled data-intensive operations, ensuring smooth performance during model training and evaluation. It demonstrated stable and smooth performance for all machine learning tasks without any drops or interruptions.

**Decision tree** Decision trees recursively partition the feature space into regions that minimize impurity, often measured by entropy for classification tasks.

Entropy Formula

$$H(T) = - \sum_{i=1}^c p(i|T) \log_2 p(i|T)$$

$H(T)$ : Entropy of node  $T$ ,  $p(i|T)$ : Proportion of samples of class  $I$  in node  $T$  and  $c$ : number of classes ( $c=2$  in this study).

In this classifier, we used the criterion of Gini score and best splitter without class weight.

**Gradient boosting** Gradient boosting combines weak learners sequentially to minimize a loss function, adjusting predictions with a learning rate of 0.001

$$\hat{y}_i^{(t+1)} = \hat{y}_i^{(t)} + \eta \cdot h^{(t)}(x_i)$$

$\hat{y}_i^{(t)}$ : Prediction of the ensemble at iteration  $t$ .

$h^{(t)}(x_i)$ : Weak learner (e.g., decision tree) prediction for sample for  $x_i$ .

**Logistic regression** Logistic regression models the probability of a binary outcome using a logistic function.

Logistic function

$$P(y = 1|x) = \frac{1}{1 + e^{-(w^T x + b)}}$$

$w$ : Coefficients (weights),  $x$ : input features,  $b$ : Bias term.

The default configuration of LogisticRegression utilized the lbfgs solver, which is well-suited for small to medium-sized datasets. It employed L2 regularization (penalty='l2') with a regularization strength of  $C=1$ . The class\_weight parameter was set to None, indicating that all classes were treated equally unless specified

otherwise. The optimization process was capped at a maximum of 100 iterations ( $\text{max\_iter} = 100$ ) to identify the optimal solution.

Loss function (binary cross-entropy)

$$L(w, b) = -\frac{1}{N} \sum_{i=1}^N [y_i \log(P(y=1|x)) + 1 - y_i \log(1 - P(y=1|x))]$$

$L(w, b)$ : Binary cross-entropy loss,  $y_i$ : Actual label of sample  $i$ ,  $P(y=1|x)$ : Predicted probability of class 1 for sample  $i$ ,  $N$ : number of samples.

**Random forest** RF constructs an ensemble of decision trees where each tree is built on a random subset of the features and a random subset of the data. In the random forest, the Gini score is used as the criterion to make the optimum efficiency of the classifier, which is demonstrated as follows:

$$Gini = 1 - \sum_{i=1}^c p_i * (1 - p_i)$$

$c$ : The number of classes in the target variable.  $p$ : The proportion (or probability) of class  $i$  in the node.

**Support vector machine (SVM) with linear kernel and probability** SVM finds a hyperplane that separates classes in the feature space, with the linear kernel indicating a linear decision boundary.

Decision function for linear SVM  $f(x) = w^T x + b$

$w$ : weight vector,  $b$ : Bias term.

Probability estimation

$$P(y=1|x) = \frac{1}{1 + e^{-f(x)}}$$

In this experiment, we used a regularization parameter ( $c = 1.0$ ), *rbf* kernel, and a decision function shape of 'ovr' (one-vs-rest) to optimize the classification process.

**K-nearest neighbors (KNN)** KNN classifies samples based on the majority class among its  $k$  nearest neighbors in the feature space. In the present study, we considered the  $K = 5$ .

Decision Rule

$$\hat{y} = \arg \max y_j \sum_{i \in N_k(x)} I(y_i = y_j)$$

$\hat{y}$ : Predicted class for the new sample  $x$ ,  $N_k(x)$  set of  $k$  nearest neighbors of  $x$ ,  $I$ : indicator function.

**Neural network** Neural networks (NN) consist of interconnected layers of neurons that learn representations of the data. In this study, the Multilayer Perceptron Classifier (MLPClassifier) was used with the following details:

Input to Hidden Layer Transformation

$$h_j = f\left(\sum_{i=1}^c w_{ij} x_i + b_j\right)$$

$x_i$ : The  $i$ -th input feature.  $w_{ij}$ : Weight connecting the  $i$ -th input to the  $j$ -th neuron.  $b_j$ : Bias term for the  $j$ -th neuron.  $f$ : ReLU Activation function.

Hidden Layer to Output Layer Transformation

$$z_k = g\left(\sum_{j=1}^m w_{jk} h_j + b_k\right)$$

$h_j$ : Output of the  $j$ -th neuron in the hidden layer.  $w_{jk}$ : Weight connecting the  $j$ -th hidden neuron to the  $k$ -th output neuron.  $b_k$ : Bias term for the  $k$ -th output neuron.  $g$ : Output activation function.

The predicted class is the one with the highest probability:

$$\hat{y} = \arg \max_k (\hat{y}_k)$$

We set  $\text{max\_iter} = 1000$  to define the maximum number of iterations for the optimization algorithm to converge. Additionally, we configured the model with a hidden layer size of 100 ( $\text{hidden\_layer\_sizes}=(100)$ ), used 'relu' as the activation function, selected the Adam solver for optimization, and applied a constant learning rate to regulate the training process.

**Evaluation metrics**

The performance of the ML was assessed using several evaluation metrics, including area under the curve (AUC), Precision, recall, accuracy, and F1 score. These metrics provided a comprehensive evaluation of the models' predictive capabilities.

AUC measures the overall performance of the classification model by evaluating the area under the receiver operating characteristic (ROC) curve. Although AUC itself does not have a simple closed-form formula, it is computed as the area under the ROC curve, which plots the true positive rate (TPR) against the false positive rate (FPR) at various threshold settings.

Precision measures the proportion of true positives among the predicted positives, and is calculated using the formula:

$$\text{Precision} = \frac{\text{TP}}{\text{TP} + \text{FP}}$$

Recall, also known as sensitivity or true positive rate, indicates the proportion of true positives among all actual positives. The formula for recall is:

$$\text{Recall} = \frac{\text{TP}}{\text{TP} + \text{FN}}$$

Accuracy reflects the overall correctness of predictions and is calculated using the formula:

$$\text{Accuracy} = \frac{\text{TP} + \text{TN}}{\text{TP} + \text{TN} + \text{FP} + \text{FN}}$$

The F1 Score provides a balance between precision and recall by considering the harmonic mean of both metrics. The formula for the F1 score is:

$$\text{F1} = 2 \times \frac{\text{Precision} \times \text{Recall}}{\text{Precision} + \text{Recall}}$$

These metrics together give a comprehensive picture of the models' performance, with AUC assessing overall performance, precision measuring the accuracy of positive predictions, recall indicating the model's ability to capture actual positives, Accuracy reflecting the correctness of predictions, and F1 Score balancing the trade-off between precision and recall.

#### *Feature selection and ablation study*

Feature importance was evaluated to identify the most influential parameters in predicting myocardial viability. Various techniques, such as permutation importance and SHapley Additive exPlanations (SHAP) values, were used to rank features. An ablation study was conducted to determine the impact of individual features on model performance. This involved systematically removing one feature at a time and observing changes in the evaluation metrics, thus highlighting the contribution of each feature to the model's predictive accuracy.

## Results

In this study, 90 patients were enrolled at the beginning, but 11 patients were excluded due to a history of previous ischemia or CABG, lack of imaging quality, inappropriate T1 and T2 mapping, and strain analysis. The remaining 79 patients underwent statistical and ML analysis. Among the enrolled patients, according to the LGE viability assessment, the left anterior descending artery (LAD) territory was viable in 52.8% of participants (47 individuals). The right coronary artery (RCA) territory was viable in 59.5% of participants (53 individuals). The left circumflex artery (LCX) territory was viable in 60.6% of participants (54 individuals). (Fig. 4; Table 1).

### Demographic characteristics of patients

The study involved participants with a mean age of 47.97 years with a standard deviation of 12.48 years. Among the participants, 83.5% (66 individuals) were male. Regarding medical conditions, 43.0% (34 individuals) had hypertension, 32.9% (26 individuals) had diabetes, and 26.5% (21 individuals) had hyperlipidemia. Additionally, 35.4% (28 individuals) were smokers.

For functional indexes, the mean value of left atrium area was  $23.56 \pm 11.97 \text{ cm}^2$ . The mean value of right atrium was  $19.99 \pm 18.31 \text{ cm}^2$ . The mean value of left ventricular ejection fraction (LVEF) was  $28.13 \pm 10.26$ . The mean value of end-diastolic volume index (EDVI) was  $131.83 \pm 62.43 \text{ ml/m}^2$ , while the mean value of end-systolic volume index (ESVI) was  $98.95 \pm 54.55 \text{ ml/m}^2$ . The mean value of left ventricular stroke volume (LVS) was  $58.91 \text{ ml} \pm 17.76$ .

Regarding the right ventricle, the mean value of right ventricular ejection fraction (RVEF) was  $44.64 \pm 12.02$ . The mean value of right ventricular end-diastolic volume index (RVEDVI) was  $78.67 \text{ ml/m}^2 \pm 38.27$ . The mean value of right ventricular end-systolic volume index (RVESVI) was  $45.52 \text{ ml/m}^2 \pm 31.30$ . Lastly, the mean value of right ventricular stroke volume (RVS) was  $54.73 \text{ ml} \pm 16.97$ . Table 2 summarizes the complete demographic and functional metrics.

### Data adjusting

Analysis of individuals with non-viable versus viable territories in LAD, RCA, and LCX showed no significant differences in clinical factors (hypertension, diabetes, hyperlipidemia, smoking) or imaging parameters (atrial areas, ventricular functions, volumes). Only age in RCA territories approached significance ( $P=0.05$ ), with viable territories showing slightly higher mean age (Table 3). In LAD territory, non-viable segments showed reduced radial and circumferential strain with elevated T1 and T2 values. RCA territory demonstrated only

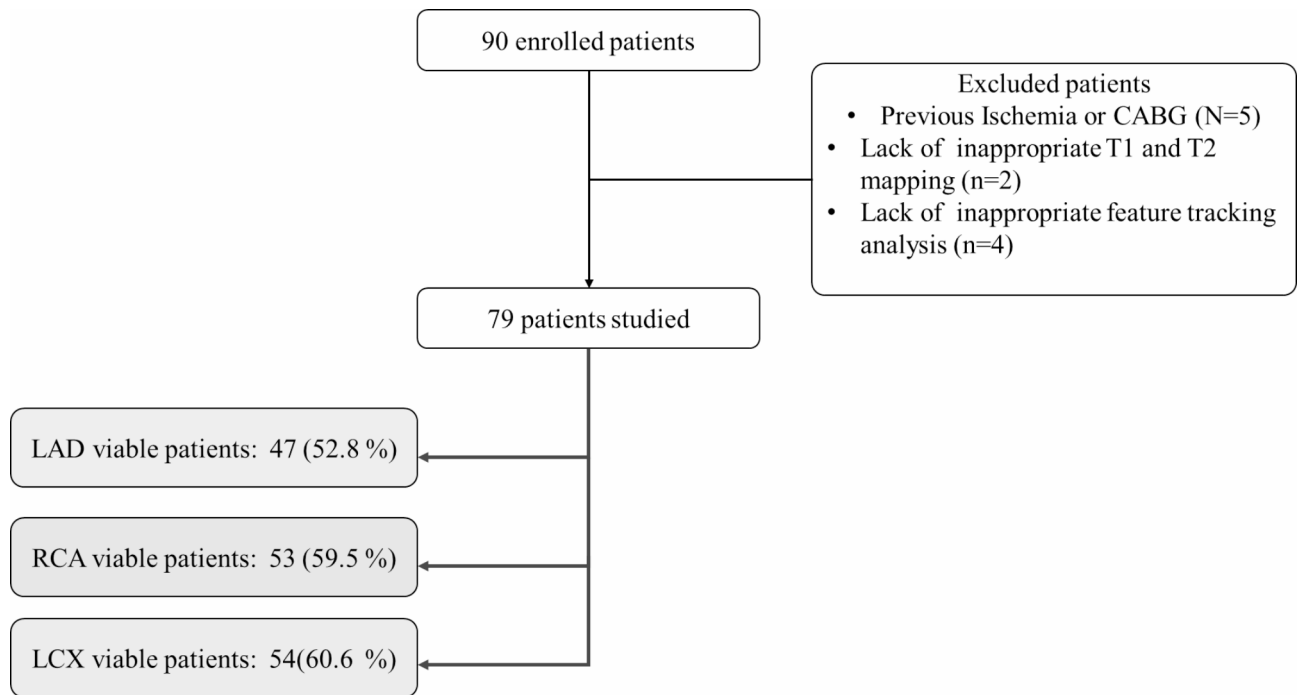


**Fig. 4.** Flowchart depicting the enrolled study population and the distribution of viable territories.

	Viable territories*	Involved segments in each territory
LAD	47 (52.8%)	58.6%
RCA	53 (59.5%)	62.5%
LCX	54 (60.6%)	64.8%

**Table 1.** Distribution of viable myocardial segments across coronary territories. \*Viable territory is defined as a territory with fibrosis involving less than 50% of the segments.

higher T2 values in non-viable areas. LCX territory exhibited lower strain values and higher T1 and T2 values in non-viable segments (Table 4; Fig. 5).

#### Evolution metrics of various models in the prediction of viability in each territory

In the LAD territory, the RF model demonstrated the highest AUC (0.87) and strong overall performance with accuracy, balanced accuracy, and F1 score of 0.74. Logistic regression also performed well, achieving an AUC of 0.83, the highest accuracy (0.78), and balanced accuracy (0.77). While the KNN model had a relatively high AUC (0.82) and accuracy (0.75), its recall was lower (0.65), though it had high precision (0.84). The NN, SVM, gradient boosting, and decision tree models showed moderate performance with varying strengths, with NN and SVM models achieving balanced accuracy and F1 scores of around 0.70–0.74. Gradient boosting and decision tree had the lowest AUCs (0.73 and 0.72, respectively), with corresponding lower metrics in other categories.

For the RCA territory, the RF model performed the best, achieving the highest AUC of 0.90 and strong overall metrics, including an accuracy of 0.79 and an F1 score of 0.78. The NN model also performed well with an AUC of 0.84, the highest accuracy of 0.81, and a balanced accuracy of 0.81, although its recall was lower at 0.69. The KNN model showed a lower AUC of 0.80 and an accuracy of 0.70, with a particularly low recall of 0.54. Logistic regression and SVM had moderate performance with AUCs of 0.76 and 0.74, respectively, and balanced accuracy around 0.72–0.73. Gradient boosting and decision tree had the lowest AUCs of 0.74 and 0.72, respectively, with corresponding lower performance metrics in accuracy and F1 score.

For the LCX territory, both the RF and NN models achieved the highest AUC of 0.92. The NN model also had the highest accuracy (0.87), balanced accuracy (0.87), recall (0.83), precision (0.90), and F1 score (0.86). The RF model followed closely with an accuracy of 0.83, balanced accuracy of 0.83, and F1 score of 0.81. Logistic regression and SVM models also performed well, with logistic regression achieving an AUC of 0.91, accuracy of 0.84, and an F1 score of 0.83, while the SVM had an AUC of 0.89, accuracy of 0.83, and an F1 score of 0.82. The KNN model had a lower AUC of 0.87 and an accuracy of 0.74, with a recall of 0.62. Gradient boosting and decision tree showed the lowest performance with AUCs of 0.76 and 0.74 respectively, and corresponding lower metrics across accuracy, balanced accuracy, and F1 scores (Table 5; Fig. 6).

Demographic characteristics	N=79
Age	47.97 ± 12.48
Gender, male	66 (83.5%)
Hypertension	34 (43.0%)
Diabetes	26 (32.9%)
Hyperlipidemia	21 (26.5%)
Smoke	28 (35.4%)
Functional metrics	
Left Atrium Area	23.56±11.97
Right Atrium Area	19.99±18.31
LVEF	28.13±10.26
LVEDVI	131.83±62.43
LVESVI	98.95±54.55
LVSV	58.91±17.76
RVEF	44.64±12.02
RVEDVI	78.67±38.27
RVESVI	45.52±31.30
RVSV	54.73±16.97

**Table 2.** Demographic characteristics and anatomical and functional metrics of the study population. Data are presented as Mean ± Standard Deviation or n (%). *LVEDVI* Left Ventricular End-Diastolic Volume Index, *LVEF* Left Ventricular Ejection Fraction, *LVESVI* Left Ventricular End-Systolic Volume Index, *LVSV* Left Ventricular Stroke Volume, *RVEDVI* Right Ventricular End-Diastolic Volume Index, *RVEF* Right Ventricular Ejection Fraction, *RVESVI* Right Ventricular End-Systolic Volume Index, *RVSV* Right Ventricular Stroke Volume.

Demographics	LAD			RCA			LCX		
	Non-viable N=32	Viable N=47	P value	Non-viable N=26	Viable N=53	P value	Non-viable N=25	Viable N=54	P value
Hypertension	17(56.66)	17(43.58)	0.18	13(56.52)	21(45.65)	0.75	11(52.38)	23(47.91)	0.53
Diabetes	13(43.33)	13(33.33)	0.56	10(43.47)	16(34.78)	0.92	10(47.61)	16(33.33)	0.36
Hyperlipidemia	11(36.66)	10(25.64)	0.78	8(34.78)	13(28.26)	0.35	4(19.04)	17(35.41)	0.36
Smoke	15(50)	13(33.33)	0.64	10(43.47)	18(39.13)	0.92	9(42.85)	19(39.58)	0.58
Age	45.96±12.64	49.41±12.44	0.24	43.92±11.19	50.04±12.82	0.05	45.52±12.54	49.07±12.53	0.26
Imaging findings									
LA area	23.32±9.87	23.74±13.64	0.88	24.56±10.55	23.03±12.85	0.61	27.06±12.96	22.04±11.45	0.10
RA area	19.04±12.62	20.71±21.98	0.70	21.26±14.68	19.30±20.29	0.66	20.13±6.75	19.93±21.62	0.96
LVEF	26.18±8.00	29.61±11.67	0.15	26.15±7.24	29.20±11.59	0.22	24.95±7.31	29.48±11.16	0.08
EDVI	136.46±78.76	128.30±48.10	0.58	122.96±46.42	136.64±70.16	0.37	147.5±65.40	125.21±61.18	0.16
ESVI	106.87±68.23	92.92±42.01	0.28	95.57±35.81	100.79±63.20	0.69	112.22±58.41	93.34±52.96	0.17
LVSV	56.78±17.14	60.58±18.47	0.37	57.32±19.28	59.75±17.26	0.58	59±16.95	58.88±18.43	0.98
RVEF	45.65±12.67	43.85±11.60	0.52	42.42±12.23	45.83±11.86	0.24	42.27±15.38	45.63±10.29	0.35
RVEDVI	81.93±45.09	76.19±32.49	0.52	79.92±33.19	78.00±41.08	0.83	87.77±50.42	74.82±31.60	0.18
RVESVI	47.84±38.47	43.76±24.85	0.58	48.53±29.83	43.89±32.26	0.54	56.36±47.67	40.94±19.86	0.15
RVSV	53.14±13.96	55.91±19.02	0.52	51.18±13.87	56.634±18.29	0.22	55±14.10	54.60±18.30	0.93

**Table 3.** Comparison of the demographic characteristics and conventional imaging findings between viable and non-viable territories. Data are presented as Mean ± Standard Deviation or n (%). *EDVI* End-Diastolic Volume Index, *ESVI* End-Systolic Volume Index, *LA area* Left Atrium area, *LVEF* Left Ventricular Ejection Fraction, *LVSV* Left Ventricular Stroke Volume, *RA area* Right Atrium area, *RVEDVI* Right Ventricular End-Diastolic Volume Index, *RVEF* Right Ventricular Ejection Fraction, *RVESVI* Right Ventricular End-Systolic Volume Index, *RVSV* Right Ventricular Stroke Volume.

CMR Parameters	LAD			RCA			LCX		
	Non-viable N=32	Viable N=47	P value	Non-viable N=26	Viable N=53	P value	Non-viable N=25	Viable N=54	P value
Longitudinal strain	7.22±4.85	9.20±5.15	0.08	5.96±4.18	7.78±4.98	0.11	4.00±5.29	7.54±5.48	0.009*
Radial strain	6.85±5.18	14.38±10.23	*0.001	9.99±6.56	13.65±9.20	0.74	13.89±7.05	19.17±10.54	0.020*
Circumferential strain	4.85±2.96	8.95±5.80	*0.001	6.84±3.50	8.76±4.72	0.07	8.16±3.81	11.84±5.12	0.002*
T1 Mapping	1076.81±97.90	1022.38±77.52	*0.01	1120.34±75.51	1136.61±398.15	0.83	1046.50±78.75	1004.09±64.65	0.014*
T2 mapping	58.60±8.21	53.65±7.95	*0.009	57.81±7.91	52.01±5.91	0.001*	56.01±8.16	51.35±6.79	0.018*

**Table 4.** T1/T2 mapping and feature tracking analysis for non-viable versus viable territories in the LAD, RCA, and LCX regions.

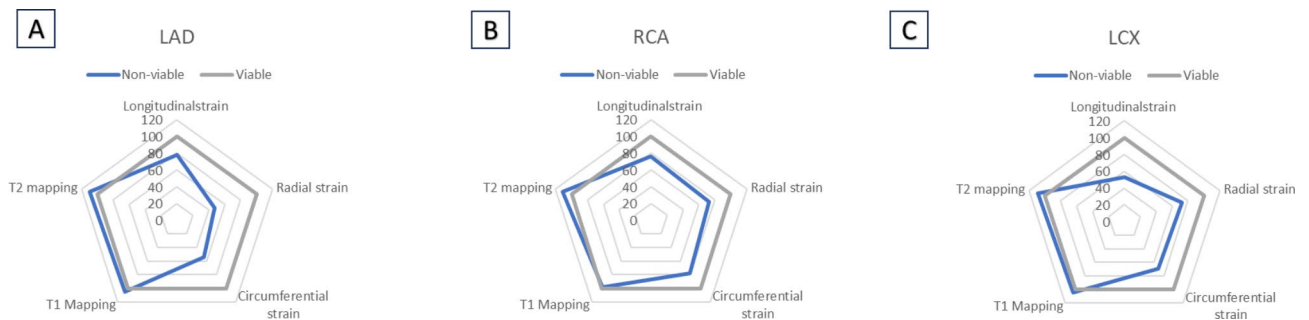


**Fig. 5.** Alteration of features in non-viable versus viable areas for each coronary territory. (A) LAD, (B) RCA, and (C) LCX.

### Model selection

Among the studied models, RF, KNN, and logistic regression demonstrated superior performance in assessing myocardial viability in the LAD territory. For the RCA territory, RF, NN, and KNN emerged as the top performers, while RF, NN, and logistic regression excelled in the LCX territory.

Analysis of feature importance, as detailed in Table 6; Fig. 7, revealed territory-specific patterns in predictive parameters. In the LAD territory, the most influential features were dominated by T2 mapping parameters from segments 13 and 14, along with segmental radial strain measurements from segments 7 and 1. The RCA territory showed a strong dependence on mapping parameters, with T2 mapping from segments 9 and 3, and T1 mapping from segment 9 emerging as key predictors. The LCX territory exhibited distinct characteristics where strain measurements played a crucial role, particularly the segmental circumferential strain of segment 11, T2 mapping of segment 6, and segmental longitudinal strain of segment 5 (Table 7).

### SHAP evaluation

SHAP evaluation was conducted to identify the most important features influencing the prediction of LGE. The obtained results align closely with the average feature importance reported in the previous section (Fig. 8).

### Discussion

In ischemic heart disease, detecting areas beyond saving is just as important as finding salvageable tissue. Thus, viability studies are now an integral part of the IHD management armamentarium<sup>16,17</sup>. Current viability studies are based on LGE as a representative marker of fibrosis and subsequent extracellular volume expansion. Other imaging properties such as T1/T2 mapping and strain analysis theoretically show changes in concert with tissue replaced by fibrosis, making them potential markers for viability assessment<sup>18–20</sup>. In contrast to LGE, in order to measure these markers, contrast injection is not needed, which enables viability study to be performed faster and safer, especially in individuals with IHD who are at increased risk of concomitant renal disease and are more likely to be unable to undergo prolonged imaging modalities<sup>21,22</sup>. In the current study, by employing multiple ML models, we tried to extract the best features for predicting the myocardial tissue viability—determined by LGE—from strain and T1 and T2 mapping values. This could provide a basis for building sophisticated prediction models of myocardial tissue viability without LGE sequences.

Prior research has shown promising results in using non-contrast CMR images as an alternative to LGE-CMR for detecting myocardial infarction, eliminating the need for gadolinium injection. Several key studies have demonstrated this potential; Baessler et al. assessed 72 patients (52 with myocardial infarction, 20 healthy controls) using radiomics features and logistic regression models, achieving an AUC of 0.93 for large infarctions and 0.92 for small infarctions<sup>9</sup>. Zhang et al.'s study of 843 myocardial infarction patients using a deep learning virtual native enhancement model showed strong correlation with LGE in scar quantification ( $R=0.89$ ) and 84%

	Model	AUC	Accuracy	Balanced accuracy	Recall	Precision	F1 score
LAD	Random Forest	0.87	0.74	0.75	0.75	0.78	0.74
	Neural Network	0.78	0.74	0.74	0.72	0.79	0.74
	KNN	0.82	0.75	0.75	0.65	0.84	0.70
	Logistic Regression	0.83	0.78	0.77	0.74	0.83	0.77
	SVM	0.79	0.72	0.72	0.70	0.77	0.70
	Gradient Boosting	0.73	0.70	0.71	0.62	0.82	0.65
	Decision Tree	0.72	0.71	0.72	0.73	0.73	0.69
RCA	Random Forest	0.90	0.79	0.79	0.77	0.81	0.78
	Neural Network	0.84	0.81	0.81	0.69	0.92	0.77
	KNN	0.80	0.70	0.70	0.54	0.81	0.62
	Logistic Regression	0.76	0.73	0.73	0.64	0.79	0.69
	SVM	0.74	0.72	0.72	0.59	0.82	0.66
	Gradient Boosting	0.74	0.66	0.67	0.65	0.72	0.65
	Decision Tree	0.72	0.71	0.72	0.65	0.78	0.67
LCX	Random Forest	0.92	0.83	0.83	0.79	0.87	0.81
	Neural Network	0.92	0.87	0.87	0.83	0.90	0.86
	KNN	0.87	0.74	0.74	0.62	0.84	0.69
	Logistic Regression	0.91	0.84	0.84	0.79	0.89	0.83
	SVM	0.89	0.83	0.83	0.78	0.88	0.82
	Gradient Boosting	0.76	0.69	0.69	0.65	0.71	0.66
	Decision Tree	0.74	0.74	0.74	0.70	0.76	0.71

**Table 5.** Evaluation metrics of various models used for predicting viability in each coronary territory. *AUC* Area Under the Curve, *KNN* K-Nearest Neighbors, *SVM* Support Vector Machine.

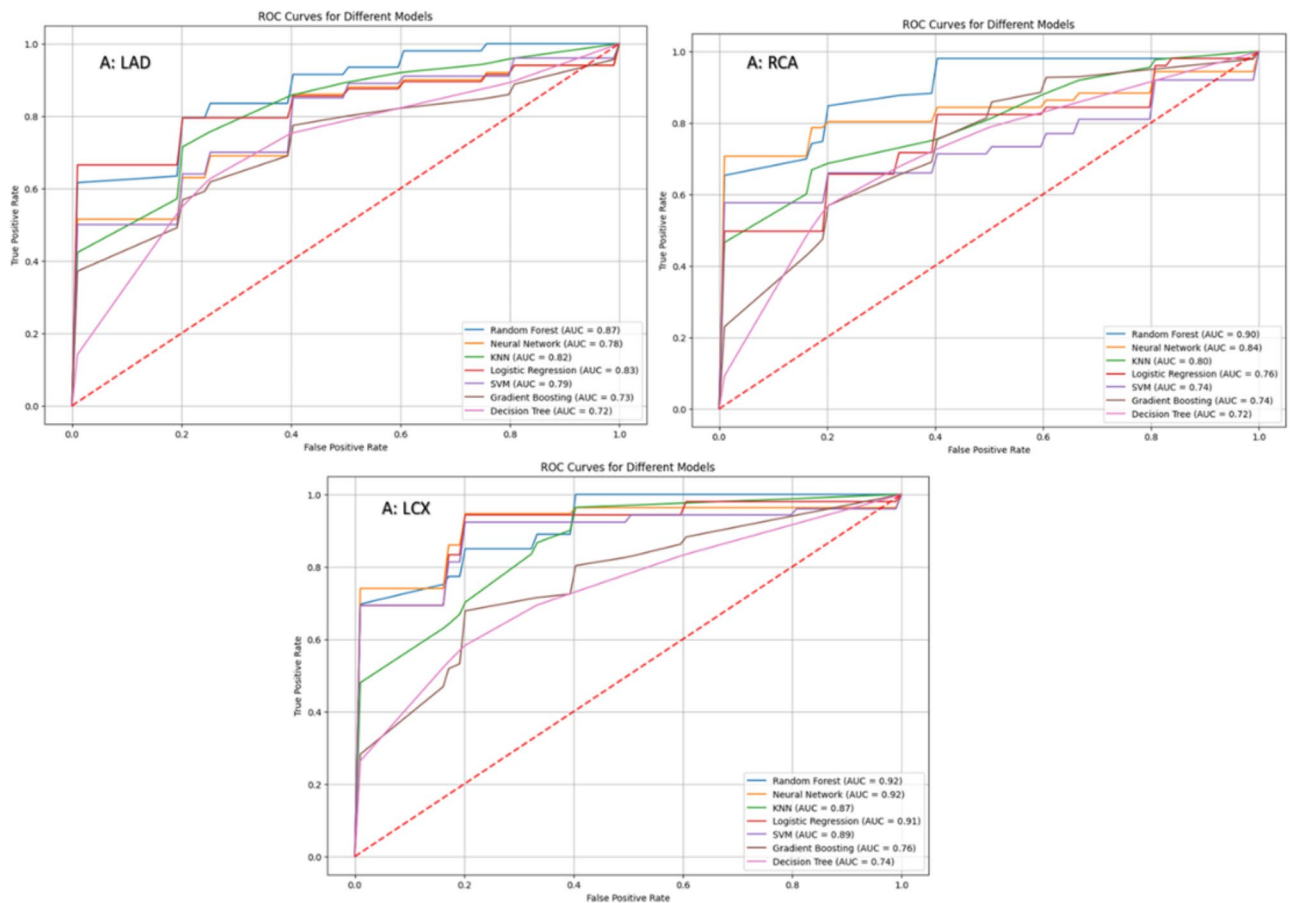


**Fig. 6.** AUC curves of various machine learning models for predicting LGE.

Feature	Logistic Regression	SVM	Gradient Boosting	Decision Tree	Random Forest	KNN	Neural Network	Average [RF, LR, KNN] <sup>1</sup>
LAD								
T2_13	0.00	0.73	0.47	0.66	1.00	1.00	1.00	0.66
SRS7	0.76	0.59	0.00	0.07	0.30	0.81	0.81	0.62
SRS1	0.68	0.46	0.51	0.39	0.37	0.59	0.59	0.55
T2_14	0.17	0.35	1.00	1.00	0.92	0.54	0.54	0.54
SCS13	0.52	0.01	0.05	0.02	0.20	0.56	0.56	0.43
SCS8	0.57	0.29	0.00	0.03	0.23	0.47	0.47	0.42
T2_global	1.00	1.00	0.42	0.35	0.26	0.00	0.00	0.42
SRS8	0.50	0.06	0.16	0.18	0.20	0.49	0.49	0.40
SCS1	0.52	0.01	0.08	0.08	0.33	0.31	0.31	0.39
T2_7	0.55	0.29	0.11	0.01	0.38	0.21	0.21	0.38
RCA								
T2_9	0.00	1.00	0.61	0.54	0.89	1.00	1.00	0.96
T2_3	0.35	0.07	0.25	0.04	0.70	0.68	0.68	0.69
T1_9	0.51	0.08	0.20	0.16	0.66	0.45	0.45	0.52
T2_4	0.21	0.57	0.20	0.14	0.46	0.40	0.40	0.42
T2_15	0.27	0.41	0.02	0.14	0.36	0.42	0.42	0.40
T1_3	0.54	0.06	1.00	1.00	1.00	0.10	0.10	0.40
SCS9	0.56	0.04	0.18	0.19	0.83	0.18	0.18	0.40
T1_4	0.63	0.06	0.27	0.24	0.91	0.12	0.12	0.39
T1_10	0.39	0.11	0.07	0.08	0.31	0.33	0.33	0.32
T1_15	0.22	0.56	0.12	0.26	0.31	0.30	0.30	0.30
LCX								
SCS11	1.00	0.95	0.88	0.69	0.78	0.64	0.64	0.81
T2_6	0.01	0.89	1.00	1.00	1.00	1.00	1.00	0.66
SLS5	0.76	0.28	0.60	0.19	0.61	0.44	0.44	0.60
IZS	0.07	0.89	0.74	0.07	0.92	0.54	0.54	0.51
T2_12	0.40	0.10	0.50	0.33	0.60	0.52	0.52	0.51
SCS16	0.58	0.10	0.60	0.14	0.59	0.29	0.29	0.49
SCS12	0.78	0.59	0.01	0.02	0.18	0.23	0.23	0.40
SRS11	0.41	0.53	0.01	0.01	0.37	0.35	0.35	0.38
SCS6	0.74	0.28	0.19	0.15	0.21	0.18	0.18	0.37
T1_5	0.14	0.80	0.21	0.10	0.56	0.41	0.41	0.37

**Table 6.** Normalized feature importance and the selection of the top 10 most important features based on the three best-performing models. *IZS* Infarct Zone Size, *KNN* K-Nearest Neighbors, *SCS* Segmental Circumferential Strain, *SLS* Segmental Longitudinal Strain, *SRS* Segmental Radial Strain, *SVM* Support Vector Machine. The numbers presented in the tables are estimated using max-min standardization. <sup>1</sup>In the evaluation of the features importance in the LAD domain, Random forest, Logistic regression and K nearest neighbor have the best performance and the average score estimate based on these models. <sup>2</sup>In the evaluation of the features importance in the LAD domain, Random forest, Neural Network and K nearest neighbor have the best performance and the average score estimate based on these models. <sup>3</sup>In the evaluation of the features importance in the LAD domain, Random forest, Neural Network and Logistic Regression have the best performance and the average score estimate based on these models.

accuracy in detecting scars<sup>2</sup>. Additional research includes Chen et al.'s study of 150 patients using a combined physiological-clinical ML model, achieving 88.67% classification accuracy<sup>23</sup>, and Xu et al.'s work with deep spatiotemporal generative adversarial networks on cine-CMR images, reaching 96.98% pixel classification accuracy<sup>24</sup>. Abdulkareem et al. analyzed 272 patients (108 with infarction, 164 controls) using U-Net and ResNet50 models, with SVM achieving accuracy scores of 0.68 and decision trees reaching 0.62<sup>25</sup>.

However, non-contrast assessment of myocardial viability across different segments and coronary territories has been limited to isolated parameter analysis and small sample sizes. Two notable studies explored this area: Dastidar et al. demonstrated excellent diagnostic accuracy using native T1 mapping compared to LGE (AUC of 0.88 in chronic MI and 0.83 in acute MI) in 60 patients<sup>7</sup>, while Tantawy et al. showed moderate diagnostic accuracy using Feature Tracking strain analysis (AUC of 0.7 for circumferential strain and 0.67 for radial strain) in 30 chronic ischemic patients<sup>6</sup>.

Hence, for the first time our study aimed to evaluate the combined efficacy of FT strain analysis and T1/T2 mapping integrated with ML pattern recognition techniques for predicting myocardial viability at both segmental and coronary artery territory levels. Notably, the assessment of coronary artery territory viability

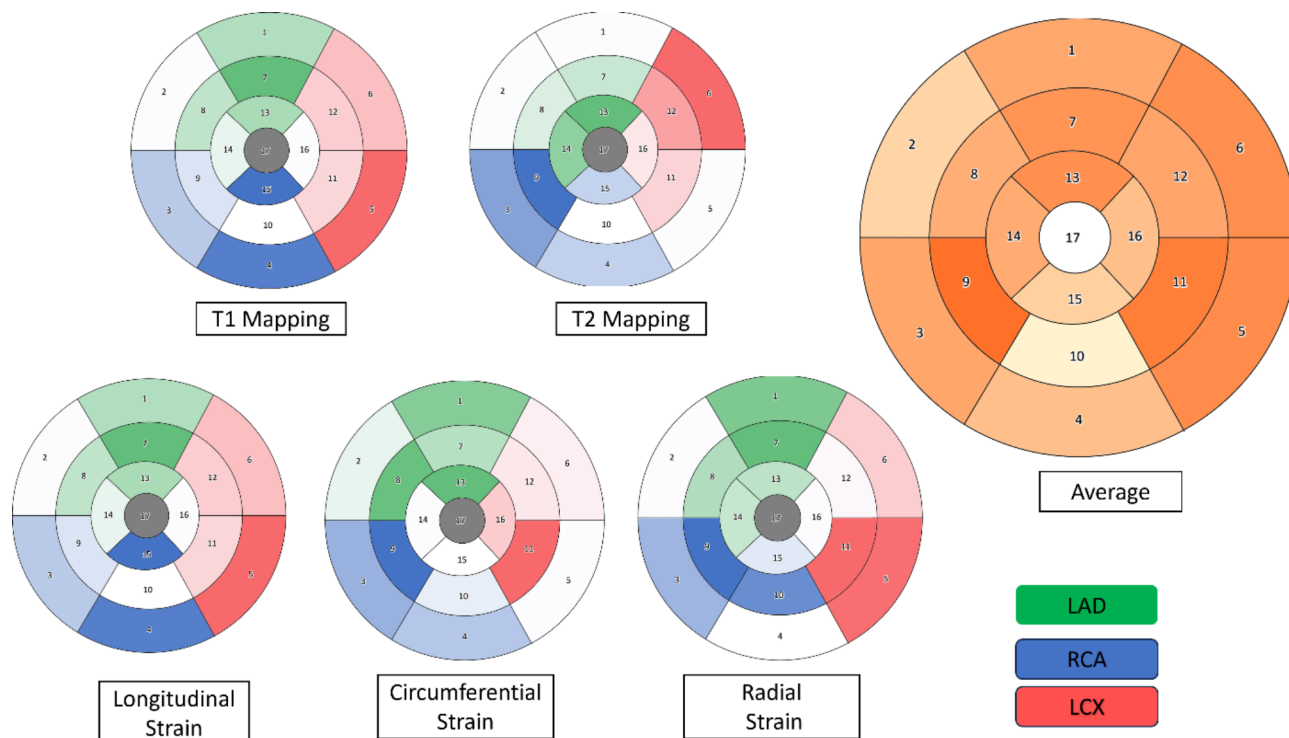


**Fig. 7.** Nomogram importance of T1/ T2 mapping and feature tracking analysis in each segment compared to other segments and features.

has not been addressed in prior studies. This analysis provides crucial information for clinical decision-making regarding revascularization strategies and risk stratification.

We found that within the LAD territory, RF, logistic regression, and KNN showed the highest discriminatory power for viability. The ten most valuable features extracted comprise various segmental radial and circumferential peak strains and T2 mapping, along with global T2 mapping. Concerning LCX territory, RF, NN, and logistic regression were the most fruitful methods. Circumferential strains of all segments were within the ten best features, while only one segment's radial and longitudinal strain was within these features. Basal T1 and basal and mid T2 were also found to be within the most effective features for viability assessment. Regarding segments supplied by RCA, RF, NN, and KNN were found to be superior. The ten most effective features only comprised T1 and T2 mapping values except for the circumferential strain of one mid-segment.

Similar to prior literature, we found the highest discriminatory value between viable and non-viable regions were circumferential and radial strains rather than longitudinal ones<sup>6</sup>. GCS and GRS showed the highest correlations with LVEF, while GLS was the least correlated global strain<sup>6,26</sup>. Moreover, the circumferential global strain is the most reproducible global strain<sup>6,27</sup>. Thus, taking circumferential strains into account for viability prediction might be more practical compared to other strain values, especially in LAD territory.

Another merit of segmental peak strains is their discriminatory value for myocardial viability assessment of their respective segments<sup>6</sup>. To the best of our knowledge, this study is the first to pursue strain and T1 and T2 mapping features to determine the myocardial viability according to coronary circulation territories. Evaluating the segmental strains and T1 and T2 mapping values based on their respective coronary territory theoretically could enhance myocardial tissue viability prediction. We found that the most valuable features differ for each coronary territory. The best extracted features for RCA territory were mostly T1 and T2 mapping, while those of LAD and LCX were mostly segmental peak strains. Possible explanation for this difference is the fact that strain values of RCA territory which is mostly comprised of right ventricle, cannot be as precisely and accurately measured as LCX and LCA territories<sup>28</sup>.

A number of studies pursued cut-points for peak strain values to discriminate viable and non-viable myocardium<sup>6,29</sup>. However, we tried to build a basis to develop a ML model composed of the best discriminatory features, taking arterial territories into account in order to attain higher accuracy. Given the complexity of myocardial tissue hibernation/stunning and viability pathophysiology, the ultimate model hypothetically surpasses the discriminatory power of a single feature.

The findings of this study demonstrate the potential of ML techniques guided by FT strain analysis and T1/ T2 mapping, to predict myocardial viability with high accuracy. This approach offers a non-contrast alternative to the traditional LGE-based method, addressing some of the limitations associated with LGE, such as contrast agents dependency and inability to enlighten functional features of myocardial tissue.

Our results indicate that ML models, particularly gradient boosting and RF, achieved high performance metrics in predicting myocardial viability, with AUC, precision, recall, accuracy, and F1 scores comparable

	SCS	SRS	SLS		T1	T2				
LAD	SCS1	0.392	SRS1	0.550	SLS1	0.200	T1_1	0.263	T2_1	0.237
	SCS13	0.432	SRS13	0.367	SLS13	0.208	T1_13	0.226	T2_13	0.667
	SCS14	0.252	SRS14	0.341	SLS14	0.144	T1_14	0.326	T2_14	0.548
	SCS2	0.275	SRS2	0.176	SLS2	0.123	T1_2	0.364	T2_2	0.241
	SCS7	0.336	SRS7	0.627	SLS7	0.278	T1_7	0.228	T2_7	0.384
	SCS8	0.427	SRS8	0.403	SLS8	0.186	T1_8	0.227	T2_8	0.334
	LCX	SCS11	0.810	SRS11	0.381	SLS11	0.289	T1_11	0.239	T2_11
SCS12		0.401	SRS12	0.190	SLS12	0.314	T1_12	0.255	T2_12	0.512
SCS16		0.492	SRS16	0.183	SLS16	0.177	T1_16	0.237	T2_16	0.319
SCS5		0.332	SRS5	0.373	SLS5	0.608	T1_5	0.376	T2_5	0.255
SCS6		0.379	SRS6	0.247	SLS6	0.359	T1_6	0.257	T2_6	0.667
RCA		SCS10	0.122	SRS10	0.246	SLS10	0.022	T1_10	0.324	T2_10
	SCS15	0.082	SRS15	0.166	SLS15	0.271	T1_15	0.302	T2_15	0.403
	SCS3	0.256	SRS3	0.211	SLS3	0.116	T1_3	0.400	T2_3	0.688
	SCS4	0.208	SRS4	0.147	SLS4	0.249	T1_4	0.385	T2_4	0.417
	SCS9	0.396	SRS9	0.269	SLS9	0.071	T1_9	0.521	T2_9	0.965

The numbers presented in the tables are estimated using max-min standardization. SCS Segmental Circumferential Strain, SLS Segmental Longitudinal Strain, SRS Segmental Radial Strain.

**Table 7.** Importance of T1/ T2 mapping and feature tracking analysis in each segment compared to other segments and features.

to those obtained with LGE<sup>30,31</sup>. This finding is consistent with previous studies that have highlighted the effectiveness of ML algorithms in cardiac imaging and viability assessment<sup>32,33</sup>. The integration of FT strain analysis and T1/T2 mapping provides a more comprehensive evaluation of myocardial tissue characteristics, potentially enhancing the diagnostic capability beyond what is achievable with LGE alone<sup>34,35</sup>.

The deep learning model, utilizing a 5-layer fully connected NN, also demonstrated strong predictive performance. This supports the growing body of evidence that deep learning techniques can effectively handle complex, high-dimensional data and uncover intricate patterns beyond the traditional methods' grasp<sup>36</sup>. Previous studies have shown that deep learning models can outperform conventional ML algorithms in various medical imaging tasks, including cardiac imaging. Our study adds to this literature by demonstrating the applicability of deep learning in the context of myocardial viability assessment.

One significant advantage of using FT strain analysis and T1/T2 mapping is the ability to provide functional and structural information about the myocardium without the need for contrast administration. This is particularly beneficial for patients with contraindications to gadolinium-based contrast agents as those with chronic kidney disease<sup>10</sup>. Moreover, these non-contrast techniques can be easily integrated into routine CMR protocols, potentially increasing their adoption in clinical practice and decrease health expenditure<sup>37</sup>. However, the application of ML and deep learning techniques requires substantial computational resources and expertise, which may limit their widespread use in clinical settings without appropriate support and infrastructure.

This study demonstrates that ML and deep learning techniques can effectively predict myocardial viability based on FT strain analysis and T1/T2 mapping data, offering a promising alternative to LGE. Future research should focus on the prospective validation of these findings, the integration of these techniques into clinical workflow, and the exploration of their potential to improve patient outcomes. This approach has the potential to provide a comprehensive, non-invasive, and patient-friendly alternative to current methods. Machine learning is increasingly essential in medical imaging diagnostics, yet it faces critical limitations that need addressing. These include the small sample size problem and the scarcity of labeled data, inefficiencies in managing multiple optimization objectives in complex diagnostic scenarios, and challenges in real-time processing of streaming medical data. Although recent studies have made significant strides in overcoming these issues, further research is necessary<sup>38–41</sup>. Besides, Deep learning architectures, especially convolutional neural networks (CNNs), have demonstrated remarkable capabilities in automatically extracting relevant features from medical images, often

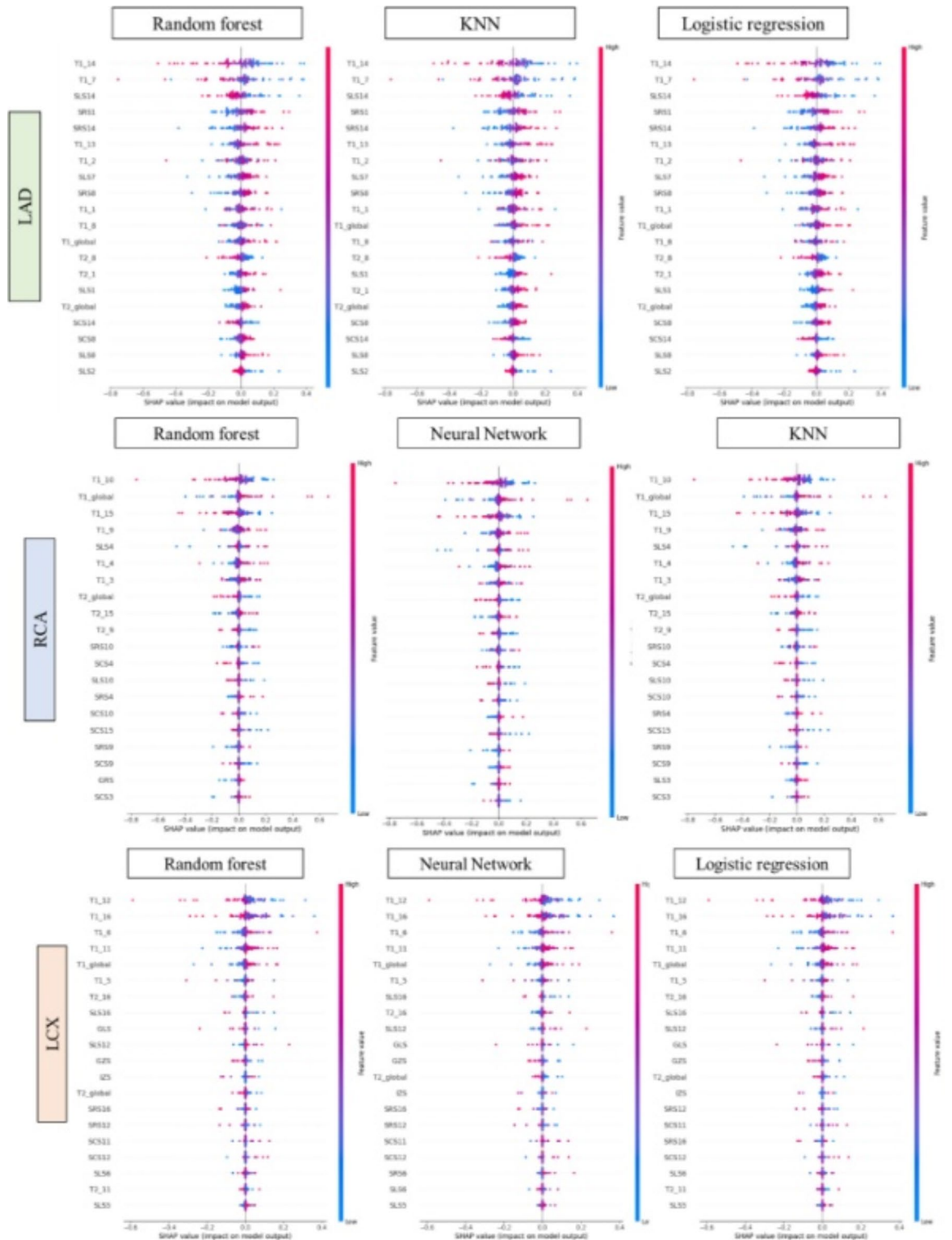


**Fig. 8.** SHAP analysis shows the importance of each feature in the top three best-performing models for predicting LGE across coronary territories.

matching or exceeding human-level performance in specific diagnostic tasks<sup>42–44</sup>, which could be further used in myocardial viability assessment.

**Limitations**

The primary limitations of our study stem from the inherent biases associated with its retrospective design and the quality of the data collected retrospectively. Although the use of SMOTE helped mitigate class imbalance,

it could not fully resolve this issue. Therefore, future prospective studies with larger, more diverse populations, utilizing a variety of MRI scanners and post-processing software, are essential to validate our findings. Notably, in this study, myocardial viability was categorized into two groups: viable and non-viable, with remote myocardial regions included in the viable category. Furthermore, the involvement of radiology specialists remains critical for accurately measuring strain and delineating ROI when applying this model.

## Conclusion

In conclusion, the study demonstrated that RF and NN models provide the highest accuracy in predicting myocardial viability across different coronary territories, with notable performance in RCA and LCX regions. The integration of non-contrast imaging techniques, including T1/T2 mapping and strain analysis, proves valuable in enhancing viability assessment. Key features from these imaging techniques significantly contribute to predictive modeling, highlighting their potential to improve diagnostic accuracy for MI. This research underscores the promise of advanced imaging combined with ML to refine cardiac viability evaluation. Further studies should consider including a more diverse patient population from multiple centers and validating the promising findings of this study in various clinical settings, using multiple MR scanners and post-processing software. Additionally, performing radiomics analyses could potentially improve the model's performance.

## Data availability

The data supporting the findings of this study are available from the corresponding author (mralimohammadzadeh@yahoo.com) upon reasonable request.

Received: 6 August 2024; Accepted: 30 December 2024

Published online: 04 January 2025

## References

- Giovanni, A. et al. Global burden of cardiovascular diseases and risk factors, 1990–2019: update from the GBD 2019 study. *J. Am. Coll. Cardiol.* **76**(25), 2982–3021 (2020).
- Zhang, Q. et al. Artificial intelligence for contrast-free MRI: scar assessment in myocardial infarction using deep learning-based virtual native enhancement. *Circulation* **146**(20), 1492–1503 (2022).
- Roes, S. D. et al. Comparison of myocardial infarct size assessed with contrast-enhanced magnetic resonance imaging and left ventricular function and volumes to predict mortality in patients with healed myocardial infarction. *Am. J. Cardiol.* **100**(6), 930–936 (2007).
- Kelle, S. et al. Prognostic value of myocardial infarct size and contractile reserve using magnetic resonance imaging. *J. Am. Coll. Cardiol.* **54**(19), 1770–1777 (2009).
- Cau, R. et al. Artificial intelligence applications in cardiovascular magnetic resonance imaging: are we on the path to avoiding the administration of contrast media? *Diagnostics* **13**(12), 2061 (2023).
- Tantawy, S. W., Mohammad, S. A., Osman, A. M., El Mozy, W. & Ibrahim, A. S. Strain analysis using feature tracking cardiac magnetic resonance (FT-CMR) in the assessment of myocardial viability in chronic ischemic patients. *Int. J. Cardiovasc. Imaging* **37**(2), 587–596 (2021).
- Dastidar, A. G. et al. Native T1 mapping to detect extent of acute and chronic myocardial infarction: comparison with late gadolinium enhancement technique. *Int. J. Cardiovasc. Imaging* **35**, 517–527 (2019).
- Cau, R. et al. Potential role of artificial intelligence in cardiac magnetic resonance imaging: can it help clinicians in making a diagnosis? *J. Thorac. Imaging* **36**(3), 142–148 (2021).
- Baessler, B. et al. Subacute and chronic left ventricular myocardial scar: accuracy of texture analysis on nonenhanced cine MR images. *Radiology* **286**(1), 103–112 (2018).
- Avard, E. et al. Non-contrast cine Cardiac magnetic resonance image radiomics features and machine learning algorithms for myocardial infarction detection. *Comput. Biol. Med.* **141**, 105145 (2022).
- Larrosa, A. et al. Differentiation between acute and chronic myocardial infarction by means of texture analysis of late gadolinium enhancement and cine cardiac magnetic resonance imaging. *Eur. J. Radiol.* **92**, 78–83 (2017).
- Amzulescu, M. S. et al. Myocardial strain imaging: review of general principles, validation, and sources of discrepancies. *Eur. Heart J. Cardiovasc. Imaging* **20**(6), 605–619 (2019).
- Schuster, A., Hor, K. N., Kowallick, J. T., Beerbaum, P. & Kutty, S. Cardiovascular magnetic resonance myocardial feature tracking: concepts and clinical applications. *Circ. Cardiovasc. Imaging* **9**(4), e004077 (2016).
- Muser, D., Castro, S. A., Santangeli, P. & Nucifora, G. Clinical applications of feature-tracking cardiac magnetic resonance imaging. *World J. Cardiol.* **10**(11), 210–221 (2018).
- Pedrizzetti, G., Claus, P., Kilner, P. J. & Nagel, E. Principles of cardiovascular magnetic resonance feature tracking and echocardiographic speckle tracking for informed clinical use. *J. Cardiovasc. Magn. Reson.* **18**(1), 51 (2016).
- Garcia, M. J. et al. State of the art: imaging for myocardial viability: a Scientific Statement from the American Heart Association. *Circ. Cardiovasc. Imaging* **13**(7), e000053 (2020).
- Virani, S. S. et al. 2023 AHA/ACC/ACCP/ASPC/NLA/PCNA Guideline for the management of patients with chronic coronary diseases: a report of the American Heart Association/American College of Cardiology Joint Committee on Clinical Practice Guidelines. *Circulation* **148**(9), e9–e119 (2023).
- Taylor Andrew, J., Salerno, M., Dharmakumar, R. & Jerosch-Herold, M. T1 mapping. *JACC: Cardiovasc. Imaging* **9**(1), 67–81 (2016).
- Hamlin, S. A., Henry, T. S., Little, B. P., Lerakis, S. & Stillman, A. E. Mapping the future of Cardiac MR Imaging: case-based review of T1 and T2 mapping techniques. *RadioGraphics* **34**(6), 1594–1611 (2014).
- Schuster, A., Hor, K. N., Kowallick, J. T., Beerbaum, P. & Kutty, S. Cardiovascular Magnetic Resonance Myocardial Feature Tracking. *Circulation: Cardiovascular Imaging* **9**(4), e004077 (2016).
- Deferrari, G., Cipriani, A. & La Porta, E. Renal dysfunction in cardiovascular diseases and its consequences. *J. Nephrol.* **34**(1), 137–153 (2021).
- Laffin, L. J. & Bakris, G. L. Intersection between chronic kidney Disease and Cardiovascular Disease. *Curr. Cardiol. Rep.* **23**(9), 117 (2021).
- Chen, Z. et al. Prediction of myocardial infarction from patient features with machine learning. *Front. Cardiovasc. Med.* **9**, 754609 (2022).
- Xu, C. et al. Segmentation and quantification of infarction without contrast agents via spatiotemporal generative adversarial learning. *Med. Image Anal.* **59**, 101568 (2020).

25. Abdulkareem, M. et al. Predicting post-contrast information from contrast agent free cardiac MRI using machine learning: challenges and methods. *Front. Cardiovasc. Med.* **9**, 894503 (2022).
26. Kihlberg, J., Haraldsson, H., Sigfridsson, A., Ebbens, T. & Engvall, J. E. Clinical experience of strain imaging using DENSE for detecting infarcted cardiac segments. *J. Cardiovasc. Magn. Reson.* **17**(1), 50 (2015).
27. Morton, G. et al. Inter-study reproducibility of cardiovascular magnetic resonance myocardial feature tracking. *J. Cardiovasc. Magn. Reson.* **14**(1), 34 (2012).
28. Lange, T. & Schuster, A. Quantification of myocardial deformation applying CMR-Feature-tracking—all about the left ventricle? *Curr. Heart Fail. Rep.* **18**(4), 225–239 (2021).
29. Becker, M. et al. Myocardial deformation imaging based on ultrasonic pixel tracking to identify reversible myocardial dysfunction. *J. Am. Coll. Cardiol.* **51**(15), 1473–1481 (2008).
30. Li, G. et al. Mapping myocardial viability using interleaved T1-T2\* weighted imaging. *Int. J. Cardiovasc. Imaging* **20**(2), 135–143 (2004).
31. Azzu, A. et al. Myocardial strain analysis by cardiac magnetic resonance 3D feature-tracking identifies subclinical abnormalities in patients with neuromuscular disease and no overt cardiac involvement. *Eur. Heart J. Cardiovasc. Imaging* **24**(4), 503–511 (2023).
32. Rouzrokh, P. et al. Machine Learning in Cardiovascular Imaging: a scoping review of published literature. *Curr. Radiol. Rep.* **11**(2), 34–45 (2023).
33. Xing, J. et al. JOINT DEEP LEARNING FOR IMPROVED MYOCARDIAL SCAR DETECTION FROM CARDIAC MRI. Proc. IEEE Int Symp Biomed Imaging, 2023. (2023).
34. Chudgar, P. D., Burkule, N. J., Kamat, N. V., Rege, G. M. & Jantre, M. N. Myocardial strain imaging using feature tracking method of Cardiac MRI: our initial experience of this Novel parameter as an additional Diagnostic Tool. *Indian J. Radiol. Imaging* **32**(4), 479–487 (2022).
35. Taylor, R. J. et al. Myocardial strain measurement with feature-tracking cardiovascular magnetic resonance: normal values. *Eur. Heart J. Cardiovasc. Imaging* **16**(8), 871–881 (2015).
36. Litjens, G. et al. A survey on deep learning in medical image analysis. *Med. Image Anal.* **42**, 60–88 (2017).
37. Pennell, D. J. Cardiovascular magnetic resonance. *Circulation* **121**(5), 692–705 (2010).
38. Fei, X., Wang, J., Ying, S., Hu, Z. & Shi, J. Projective parameter transfer based sparse multiple empirical kernel learning machine for diagnosis of brain disease. *Neurocomputing* **413**, 271–283 (2020).
39. Shi, B. et al. Prediction of recurrent spontaneous abortion using evolutionary machine learning with joint self-adaptive sime mould algorithm. *Comput. Biol. Med.* **148**, 105885 (2022).
40. Chen, M.-R., Zeng, G.-Q. & Lu, K.-D. A many-objective population extremal optimization algorithm with an adaptive hybrid mutation operation. *Inf. Sci.* **498**, 62–90 (2019).
41. Jin, X., He, T. & Lin, Y. Multi-objective model selection algorithm for online sequential ultimate learning machine. *EURASIP J. Wirel. Commun. Netw.* **2019**, 1–7 (2019).
42. Zeng, N. et al. DPMSN: a dual-pathway multiscale network for image forgery detection. *IEEE Trans. Industr. Inf.* (2024).
43. Xiong, B. et al. TranSEMG: a Trans-Scale Hybrid Model for High-Accurate Hip Joint Moment Prediction. *IEEE Trans. Instrum. Meas.* (2024).
44. Wen, W. et al. Enhanced multi-label cardiology diagnosis with channel-wise recurrent fusion. *Comput. Biol. Med.* **171**, 108210 (2024).

## Acknowledgements

The authors wish to express their sincere gratitude to the Rajaie Cardiovascular Medical and Research Center, Department of Radiology, for providing the invaluable data used in this study. Special thanks are extended to Dr. Maedeh Dastmardi and Dr. Ghazaleh Salehabadi for their invaluable support and assistance throughout the research process.

## Author contributions

A.G.J. contributed to data formal analysis and writing - original draft. A.S. and K.H. contributed to data curation. M.M.B. and P.P. contributed to writing - review & editing. A.A. contributed to visualization. Conceptualization was carried out by A.M.

## Declarations

### Competing interests

The authors declare no competing interests.

### Declaration of generative AI in scientific writing

During the preparation of this work the authors used Grammarly and ChatGPT in order to correct the text and make it fluent. After using this tool/service, the authors reviewed and edited the content as needed and take full responsibility for the content of the publication.

## Additional information

**Correspondence** and requests for materials should be addressed to A.M.

**Reprints and permissions information** is available at [www.nature.com/reprints](http://www.nature.com/reprints).

**Publisher's note** Springer Nature remains neutral with regard to jurisdictional claims in published maps and institutional affiliations.

**Open Access** This article is licensed under a Creative Commons Attribution-NonCommercial-NoDerivatives 4.0 International License, which permits any non-commercial use, sharing, distribution and reproduction in any medium or format, as long as you give appropriate credit to the original author(s) and the source, provide a link to the Creative Commons licence, and indicate if you modified the licensed material. You do not have permission under this licence to share adapted material derived from this article or parts of it. The images or other third party material in this article are included in the article's Creative Commons licence, unless indicated otherwise in a credit line to the material. If material is not included in the article's Creative Commons licence and your intended use is not permitted by statutory regulation or exceeds the permitted use, you will need to obtain permission directly from the copyright holder. To view a copy of this licence, visit <http://creativecommons.org/licenses/by-nc-nd/4.0/>.

© The Author(s) 2024